The Astrophysical Journal, 804:126 (9pp), 2015 May 10 doi:10.1088/0004-637X/804/2/126

FEASIBILITY OF HELIOSPHERIC IMAGING FROM NEAR EARTH

C. E. DeForest and T. A. Howard
Southwest Research Institute, 1050 Walnut Street, Suite 300, Boulder, CO 80302, USA
Received 2015 January 4; accepted 2015 March 9; published 2015 May 11

ABSTRACT

Imaging solar wind structures via Thomson scattered sunlight has proved important to understanding the inner heliosphere. The principal challenge of heliospheric imaging is background subtraction: typical solar wind features are fainter than the zodiacal light and starfield by 2-3 orders of magnitude. Careful post-processing is required to separate the solar wind signal from the static background. Remnant background, and not photon noise, is the dominant noise source in current *STEREO* data. We demonstrate that 10× shorter exposure times would not strongly affect the noise level in these data. Further, we demonstrate that current processing techniques are sufficient to separate not only the existing background of the *STEREO* images but also diffuse variable backgrounds such as are expected to be seen from low Earth orbit. We report on a hare-and-hounds style study, demonstrating blind signal extraction from *STEREO*/HI-2 data that have been degraded by the addition of large-scale, time-dependent artifacts to simulate viewing through airglow or high-altitude aurora. We demonstrate removal of these effects via image processing, with little degradation compared to the original. Even with as few as three highly degraded source images over 48 hr, it is possible to detect and track large coronal mass ejections more than 40° from the Sun. This implies that neither the high altitude aurora discovered by *Coriolis*/SMEI, nor airglow effects seen from low Earth orbit, are impediments to a hypothetical next-generation heliospheric imager in low Earth orbit; and also that post-processing is as important to heliospheric image qualitiy as are optical contamination effects.

Key words: atmospheric effects – instrumentation: miscellaneous – methods: data analysis – solar wind – techniques: photometric

1. INTRODUCTION

Heliospheric imaging has come of age. The theory of wide-angle Thomson scattering is well understood (Vourlidas & Howard 2006; Howard & Tappin 2009; Howard & DeForest 2012a), the SMEI instrument has demon strated wide-field imaging from Earth orbit and made sev eral important breakthroughs (Eyles et al. 2003; Howard et al. 2013), and the *STEREO*/HI-2 instrument (Eyles et al. 2009) has been used to track coronal mass ejections (CMEs; e.g., Jackson et al. 2006; Harrison et al. 2008; Lugaz et al. 2008; Davis et al. 2009; Möstl et al. 2010; Wood et al. 2011; Howard & DeForest 2012b; DeForest et al. 2013), CIRs (Rouillard et al. 2008; Sheeley et al. 2008; Tappin & Howard 2009), blobs (Sheeley et al. 1997; Sheeley & Rouillard 2010), and other types of features (DeForest et al. 2012). Recent work on HI-2 background subtraction (DeForest et al. 2011) has enabled essentially complete separation of the starfield from the heliospheric imaging signal in the static deep-space environment where *STEREO* flies. But Earth-orbiting instruments such as SMEI are subject to a variable background signal independent of the starfield. This background includes the high-altitude aurora that was discovered with SMEI (Mizuno et al. 2005).

Deep space heliospheric imagers are subject to three major classes of background contamination, each of which is approximately stationary in a particular reference frame: stray light (instrument frame), zodiacal light (heliospheric frame), and starfield (celestial frame). In nominal *STEREO* operations, the first two reference frames are the same and the first two sources of contamination may be removed in one step. For an instrument closer to Earth, such as *Coriolis*/SMEI or a hypothetical Earth-orbiting heliospheric imager, it is necessary to consider a fourth source of contamination in the terrestrial frame. The main nontrivial sources of terrestrial contamination are high-altitude aurora and airglow, both of which can inject a bright diffuse illumination. These sources have, variously, been reported in units of the mean solar brightness $B_{\odot}$ (approximately 2.3×10^7 W m^{-2} SR^{-1}), S_{10} (the radiance of one 10th-magnitude star per square degree, or about 9.0×10^{-9} W m^{-2} SR^{-1}), and Rayleighs (spectral radiance: 1 R = 227 S_{10} Å^{-1}). For definitions and history of these units see, e.g., Roach (1973). While we mention S_{10} units in this introduction for convenience, we use only $B_{\odot}$ in subsequent sections.

High-altitude aurora, discovered with SMEI, have brightnesses of intrinsic radiance of order 200–300 S_{10}, or about 10^{-13} $B_{\odot}$ (Mizuno et al. 2005), comparable to the brightness of the zodiacal light. SMEI was degraded by aurora in part because its detectors were long and narrow, approximating linear slits, and the spacecraft rotated just once per orbit, affording only a single chance in each orbit to image a particular celestial direction. The high altitude aurora appears localized in space (Mizuno et al. 2005), so that it could in principle be avoided by collecting full 2D images of the sky in each location in orbit and rejecting contaminated copies of a given line of sight.

A more challenging issue is diffuse brightness—natural airglow, spacecraft ram airglow, and geocorona. Natural airglow is caused by ionization of sodium and oxygen in the ionosphere and low thermosphere, and is typically of order 200 S_{10} from the ground (Jursa 1985, Chapter 13). Spacecraft in low Earth orbit (LEO) are above the 80–100 km altitude where most natural airglow is produced (e.g., Jursa 1985). Visible light ram airglow seen from spacecraft in LEO arises primarily from a halo of recombining ions from impact-ionized material that has interacted with the spacecraft itself (e.g., Weinberg et al. 1975). Away from high-altitude aurora in a 10 m scale spacecraft, overhead brightness from 500 km LEO, due mostly to ram effects, may be as little as a few $\times 10^{-17}\,B_{\odot}$ (DeForest & Howard 2013) based on scaling from UV observations near the *Hubble Space Telescope* (*HST*; Brown et al. 2000). Direct measurements of total sky brightness (including ram airglow and the starfield) exist from the 10-color photometer on *Skylab* in 235 km LEO (Weinberg et al. 1975), and are of order 200 S_{10} (Sparrow et al. 1977). Of this brightness, up to ~50 S_{10} (~$2 \times 10^{-14}\,B_{\odot}$) may be attributed to local ram effects from *Skylab* itself and the remainder to starfield. The failure of Weinberg's 10-color photometer on *Skylab* is mentioned obliquely by Jackson et al. (2010) in justifying SMEI's requirement for high-altitude (~800 km) orbit, and we verified (B. V. Jackson 2014, private communication) that in fact this was the instrument referred to. But the failure of the 10-color photometer was mechanical, not fundamental (Sparrow et al. 1977), and despite the yet higher brightness of the zodiacal light and starfield, both Jackson & Leinert (1985) and DeForest et al. (2011) have succeeded in extracting the heliospheric Thomson scattering signal from *Helios* data and *STEREO* data, respectively. These considerations require a careful study of whether airglow from LEO is in fact a serious difficulty as implied by Jackson et al. (2010), in light of the four decades of advance in instrument and image processing technology since *Skylab* was built.

In this article, we explore the limits of a posteriori image processing to enable heliospheric imaging of interplanetary Thomson scattered light, from a viewpoint in the terrestrial or near-terrestrial environment. In particular, we consider the effect of a short (few minute) exposure time from instruments comparable to *STEREO*/HI; the effect of a strong and variable diffuse ram glow up to ~4× worse than ram effects at *Skylab* and ~1000× worse than ram effects at the *HST*; and, as an extreme limiting case, whether it is possible in principle to image heliospheric features from the ground. We carried out these studies by degrading an image sequence from *STEREO*/HI-2: by adding either shot noise to simulate a shorter exposure, or a variable diffuse signal to simulate airglow or ram glow effects. We then attempted to extract a useful signal from the data to characterize the resulting processed image quality that may be extracted under different observing conditions. The degradation and restoration were performed in a blind fashion: Howard degraded the data and gave the degraded data to DeForest for restoration. We did not discuss the degradation of specific prepared data sets.

Two additional considerations are applicable to any heliospheric imager in LEO, that are not applicable in deep space: the Earth's Moon, which can yield an additional directional source of stray light, and particle hits from the South Atlantic Anomaly and the polar regions of near-Earth space. Both of these sources have instrument-specific solutions and we therefore do not consider them in detail here. The Moon's light can be mitigated through a combination of baffling and observation timing, and the importance and strategy of this mitigation depends on the application of a particular instrument —although we note that in certain cases stray light from the Moon might have similar characteristics to the time variable diffuse glow that we do consider here. Particle hits yield time-dependent detector spikes and/or down time for the instrument itself, depending on the specific technology used for imaging. Strategies to mitigate the effects of particle showers are not specific to heliospheric imagers, so we do not consider them here.

In Section 2 we describe the source data set we used for all the studies. In Section 2.1 we describe the techniques we used to degrade a *STEREO*/HI image sequence to simulate the effects under study. In Section 3 we report the results of blind a posteriori analysis of the degraded images. Section 3.1 treats removal of variable airglow at various brightness levels; Section 3.2 treats increased photon noise from shorter exposures; and Section 3.3 treats the hypothetical case of a ground-based imager. We conclude with a short discussion of the relative importance of dark viewing conditions versus correct post-processing to future heliospheric missions.

2. DATA SET

Our objective was to simulate degraded atmospheric heliospheric image data in a controlled "laboratory" environment, so as to ascertain the level of degradation tolerable for feature detection. We therefore began with a real dataset and introduced artifacts to simulate degradation. We have selected heliospheric images from *STEREO* (HI-2A), as they already contain the first two degradation elements listed in Section 1 (zodiacal light and starfield), leaving us only to introduce the remaining two (airglow and exposure time). We selected the CME that occurred on 2008 December 12 as a well-known and well-studied feature (e.g., Davis et al. 2009; Byrne et al. 2010; Lugaz 2010; Liu et al. 2010; Howard & DeForest 2012b; DeForest et al. 2013). Additionally, DeForest et al. (2011) have quantified the zodical light and starfield in this dataset using post-processing techniques.

We began with the *STEREO*/HI-2 A L0 dataset from 2008 December 10 to December 19 inclusive, and produced L1 data using the Solarsoft *secchi_prep* routine. We included all HI-2 synoptic images in that time range. L1 processing includes flat fielding, pointing calibration, and deconvolution to remove streaks caused by shutterless operation of the instrument. These steps are described by Eyles et al. (2009). The primary post-processing we used is that described by DeForest et al. (2011); an example is given in Figure 1.

To simulate degradation by airglow, we added a separate, slowly varying digitally generated glow or "gradient" image to each data frame. Each gradient image had a radiance that depended on radial distance from a centroid location outside the actual image. This produced a gentle gradient, with nonzero curvature, across the image field. The location of the centroid was different for each image, but it was always outside the field of view (FOV). To simulate degradation by photon counting noise from a short exposure time, we introduced simulated random shot noise to each image. In this controlled environment, we could investigate independently the effects of airglow with different boundaries and gradient magnitudes, and of exposure time variation.

2.1. Contamination by Variable Diffuse Glow

We considered the effect of variable diffuse glow on analysis of a timeseries of heliospheric images. The images from *STEREO* are collected well outside Earth's environment, which contaminates deep field imagery collected near the planet. We mocked-up airglow and/or orbital ram effects with a simple

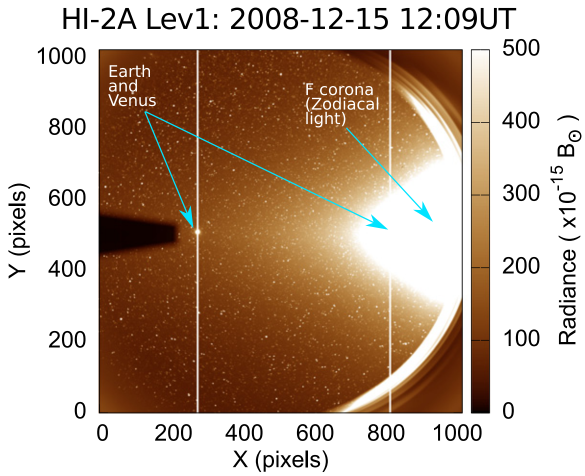

Figure 1. Sample HI-2 data frame shows the processing pipeline developed by DeForest et al. (2011). See also the digital movie included in the online version of this article. Left: Level 1 image shows stars and zodiacal light. Right: Level 2 image reveals a CME, solar wind features, and artifacts associated with planets.

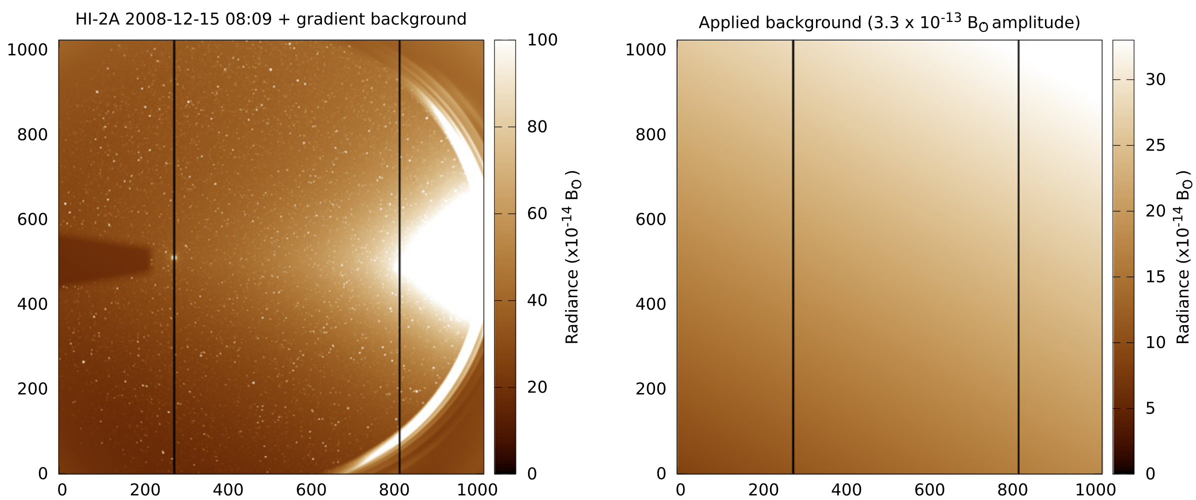

Figure 2. Sample diffuse gradient contamination in a HI-2 frame. The gradient-contaminated sets used randomly chosen centers, gradients, and amplitudes of the diffuse glow to simulate a non-simple time-variable effect such as might be seen from LEO. Left: a degraded image from HI-2 A. Right: the background applied to this particular image.

diffuse background that varied on a per-frame basis. The smooth background was not a trivial linear gradient image, which would have been equally trivial to find and remove. Instead we used a slightly curved gradient image, with independent randomly selected characteristics for each image. We chose this protocol because it is more challenging than the slowly varying effects expected from orbital ram glow and terrestrial airglow.

For each image in the sequence we selected a center pixel coordinate outside the FOV and generated an image consisting of radial distances relative to that center. The angle and radius were chosen by sampling a uniform random variable and scaling to the range of 0–2π radians or 1500–2500 pixels, respectively. We generated two values $G_{\min}$ and $G_{\max}$ by sampling uniform random variables over the top third and bottom third of the desired gradient brightness range, respectively—for example, to generate a background with a brightness range of 1.2×10^{-13}–$2.4 \times 10^{-13}\, B_\odot$, we generated $G_{\min}$ in the range 1.2×10^{-13}–$1.6 \times 10^{-13}\, B_\odot$ and $G_{\max}$ in the range 2.0×10^{-13}–$2.4 \times 10^{-13}\, B_\odot$. (These relative dynamic ranges are consistent with the results of Sparrow et al. 1977.) Then we linearly scaled the circular image onto the range $G_{\min}$–$G_{\max}$, and added the resulting scaled gradient image to the original data. We used a different randomly chosen central point, a different $G_{\min}$, and a different $G_{\max}$ for each frame of the time series. A single frame from this process is shown in Figure 2.

We considered three different sets of gradient-degraded data. Each set had a base gradient value of 1.2–2.4 as described above, scaled by a "nominal background level" of $10^{-15}\, B_\odot$, $10^{-14}\, B_\odot$, or $10^{-13}\, B_\odot$.

The selection of *randomly varying* backgrounds, rather than correlated backgrounds, was made because the challenging aspect of airglow or ram glow removal is its variability from frame to frame. Glow near a real LEO spacecraft may be represented mathematically as the sum of a fixed component, a slowly varying component, and a rapidly varying component. Fixed and sufficiently smoothly varying components are easily scrubbed by the steps described by DeForest et al. (2011), so that from a signal-processing standpoint the most challenging part of a diffuse background is the most rapidly varying portion.

2.2. Contamination by Photon Noise

After addition of the diffuse background, and also independently of the diffuse analysis, we degraded each image with simulated photon noise representative of either the full exposure time (including photons from the diffuse contamination added as in Section 2.1) or a shorter exposure. First, we converted the original or gradient image from mean solar brightnesses to photons. We estimated the deposited energy via the formula $E_{\mathrm{pix}} = B_{\odot} A_0 Q \delta t \Omega_p B_{\mathrm{pix}}$ (with $B_{\odot}$ the mean solar radiance; A_0 the area of the HI-2 aperture; Q an estimated overall quantum efficiency, conservatively estimated at 42%; δt the exposure time of a HI-2 image; Ω_p the subtended solid angle of a pixel; and B_{pix} the reported radiance in an image pixel). We scaled the deposited energy according to a modified exposure time estimate: $E'_{\mathrm{pix}} \equiv E_{\mathrm{pix}}\, \delta t' \delta t^{-1}$. We then calculated the per-pixel photon count $N_{\mathrm{pix}} \equiv E'_{\mathrm{pix}} / E_{\mathrm{ph}}$ for each pixel, using the familiar relationship $E_{\mathrm{ph}} = \mathrm{hc}/\lambda$ and an assumed typical wavelength λ of 450 nm. These assumptions are conservative and should produce a slight *overestimate* of the photon noise in the actual instrument: the HI-2 instruments, as built, have central wavelengths closer to 600 or 700 nm, and the overall quantum efficiency may be a factor of two higher than we assumed (Eyles et al. 2009).

We generated a shot noise image by sampling a uniform random variable on the domain $-N_{\mathrm{pix}}^{0.5}$ to $N_{\mathrm{pix}}^{0.5}$ for each pixel of the image, and added this shot noise to the image. The uniform random variable provides a slightly pessimistic approximation of the true Poisson statistics of photon noise.

For reference, the zodiacal light near the inner portion of the HI-2 FOV has a radiance of $10^{-13} B_{\odot}$. Using the published aperture of 7 mm diameter and overall efficiency described by Eyles et al. (2009), and mean solar radiance of 2×10^7 W m^{-2} SR^{-1}, we derive a photon count rate of 1.7×10^3ph s^{-1} deg^{-2} in that portion of the focal plane, or 1.2×10^8 ph deg^{-2} in a single 5000 s exposure. This corresponds to an a priori relative photometric error of 1×10^{-4} ($1 \times 10^{-17} B_{\odot}$) in each square degree, due to photon counting statistics alone, in the brightest portion of the image. The HI-2 detector has 2 arcmin pixels, but they are binned 2×2 to 4 arcmin in the downlinked data stream. These "L1 pixels" subtend 4.3×10^{-3} deg^2 (Eyles et al. 2009), and therefore the photon counting noise in each pixel, considered separately, is approximately 25× higher than the noise level in each square degree: $2.5 \times 10^{-16} B_{\odot}$ in one L1 pixel. We note, but neglect, the known order-of-25% variation in pixel solid angle across the HI-2 FOV.

To simulate the effect of a shorter exposure, 510 s, we added noise to each L1 pixel of a test HI-2 sequence. We scaled the noise added to each pixel using the relation:

$$\sigma_{\mathrm{pix}} = \left(\sqrt{\frac{5000}{510} \frac{B_{\mathrm{pix}}}{10^{-13} B_{\odot}}}\right) \left(2.5 \times 10^{-16} B_{\odot}\right), \qquad (1)$$

where σ_{pix} is the standard deviation (rms value) of the noise added to a particular pixel, and B_{pix} is the instrument-reported brightness (radiance) of that pixel. We simulated this additional Poisson noise with a uniform distribution with the correct standard deviation, calculated and then sampled for each pixel throughout the data set.

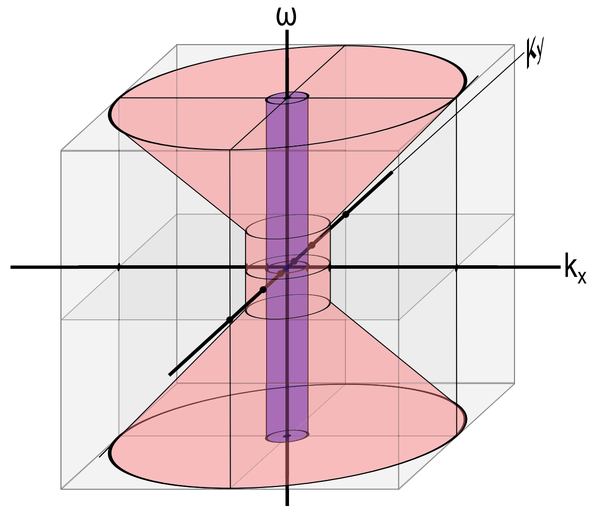

Figure 3. Fourier motion filter is the penultimate stage of processing for *STEREO*/HI-2 images. Image features outside the pink cone are rejected. To reject variable diffuse backgrounds, we also reject features inside the purple cylinder.

3. ANALYSIS

We treated separately the two types of degradation, to assess how well we could reproduce the heliospheric signal with the less-than-ideal data degraded as in Section 2.1.

3.1. Analysis of Gradient-contaminated Images

STEREO/HI-2 background subtraction has been described in detail by DeForest et al. (2011). Here, we summarize the process and describe how we modified it to deal with the variable bright background described in Section 2.1. A full 7 day set of *STEREO*/HI-2 images are assembled into a data cube, with three independent variables: detector-X (image position), detector-Y (image position), and frame number (time). A low percentile (generally 4) value of the pixel is taken to be the value of the zodiacal light, and is subtracted from the time series. The instrument distortion and orbital evolution functions are inferred from cross-correlation of the starfield in two of the images, and this measured parameterized distortion function is used to resample all the images to fix (freeze) the celestial sphere. The distortion function is tweaked with a small starfield jitter correction for each image. In the celestial coordinate system, the minimum value of each pixel is subtracted, and the image is 11×5 median-filtered to remove residual stellar artifacts (which are due to small misalignments, to nonlinearities in the detector, and to variations in the pointspread function across the field). Then each pixel is again treated as a timeseries, and a cubic polynomial is fit to it and subtracted from the timeseries. The resulting reduced celestial-frame cube is motion-filtered using a modified conic filter function to reject slow moving features (Figure 3). This pipeline is modified as follows.

The zodiacal light minimization step is corrupted by our added bright, diffuse background. We better approximate this background with a multistep process. First, the 4 percentile, i.e., near-minimum, value of each pixel is identified and removed just as in the original process. Then a smooth background is created for each image by replacing each pixel with the 1 percentile value of its 33×33 pixel neighborhood. We chose this size "by eye" as larger than most CME fronts but small enough to approximate the background gradients well. The 1 percentile value (the 10th lowest value in the collection of 1089 pixels in the neighborhood) is used to prevent an occasional outlier pixel from damaging a complete neighborhood. We call this process *minismoothing* for convenience. We further smooth this background by convolving it with a 100-pixel full-width Gaussian of revolution. Subtracting this convolved, minismoothed background, and reprocessing through the F corona minimizer reduces the applied variable diffuse background by a factor of 10–30. We resample to celestial coordinates, null the stellar background, and perform 11×5 median smoothing exactly as in DeForest et al. (2011). We carry out a second minismoothing round with the nulled data, then re-null using the same algorithm, and fit (and remove) a polynomial trend from the time series of each pixel, again, exactly as in DeForest et al. (2011). This second minismoothing round reduces the smooth component of the background by another factor of order 10, and is important because at this stage the background is being discriminated primarily via its large spatial scale (diffuse nature). All these steps together reduce the variable, diffuse background by a factor of 100 below its original level, but it is still comparable to the signal of interest, in the frames with $\sim 10^{-14}\,B_\odot$ applied background levels.

The additional noise still remaining in the signal takes the form of rapidly fluctuating, diffuse (~100 pixel scale) patches of image, whose size arises from the spatial crossover imposed by the 100 pixel Gaussian smoothing. These residual background patches are, fortunately, characterized by a particular location in Fourier space (Figure 3): they have low spatial frequencies k and high temporal frequencies ω. In DeForest et al. (2011), we describe a motion filter that rejects slow-moving residual artifacts from the nulling process; for the degraded-image analysis we also reject the low-k, high-ω portions of the data as well.

Figure 4 shows the results of the modified processing, applied to image sequences degraded with randomized background gradients at three levels: $10^{-15}\,B_\odot$, $10^{-14}\,B_\odot$, and $10^{-13}\,B_\odot$. Non-degraded images yield slightly worse results than the standard pipeline, but similarly clear CME images. The $10^{-15}\,B_\odot$ gradient level leaves the results essentially unchanged. At the $10^{-14}\,B_\odot$ gradient level, about $10\times$ brighter than the CME itself, the results are but slightly degraded; and at $10^{-13}\,B_\odot$ the gradient overwhelms the simple filtration we describe here.

We conclude that the simple modifications, described above, to our existing background subtraction algorithm are sufficient to process heliospheric imagery even in the presence of highly variable, diffuse backgrounds at levels up to a few $\times 10^{-14}\,B_\odot$. In particular, this technique reduces such variable diffuse backgrounds by a factor over 100, enabling bulk photometry of a typical CME at the 10% level even in the presence of variable diffuse backgrounds $10\times$ stronger than the CME itself. This result is important because existing techniques, including our earlier work (DeForest et al. 2011), have relied on the static nature of the diffuse background; while here we only make use of its different location in (k_x, k_y, ω) inverse space, from the information of interest.

3.2. Analysis of Images with Short Exposure

To identify the role of exposure time in the original data set, we reduced photon-noise-degraded images using the same processing steps as the original HI-2 image data (described by DeForest et al. 2011). We compared the original images, with 5000 s integration time, to photon noise degraded images with the equivalent of 510 s of exposure exposure time. We calculated the noise level by examining the difference between two adjacent-in-time images in a location and time away from any obvious bright solar wind features. The difference image samples the noise field twice, so (taking the noise values themselves to be uncorrelated between frames) its rms value is $\sqrt{2}$ times the noise field. We measured an rms value of $6.9 \times 10^{-17}\,B_\odot$, which corresponds to a noise level of $4.9 \times 10^{-17}\,B_\odot$, in the original exposure sequence. The HI-2 pipeline includes a smoothing filter that is 11×5 pixels or $0.23\ \mathrm{deg}^2$—so this value indicates a photon noise level of $3.7 \times 10^{-16}\,B_\odot$ in one L1 pixel, or $2.4 \times 10^{-17}\,B_\odot$ in each $1\ \mathrm{deg}^2$ area. Degrading the image as described in Section 2.1 yielded an rms difference value of $7.1 \times 10^{-17}\,B_\odot$, corresponding to a noise level of $2.5 \times 10^{-17}\,B_\odot$ in each $1\ \mathrm{deg}^2$ area. In turn, this indicates that the image noise level is dominated by terms other than photon noise. Subtracting the two terms in quadrature yields a noise level difference of $6 \times 10^{-18}\,B_\odot$ in each $1\ \mathrm{deg}^2$ area between the two cases. This is consistent with the estimated total photon noise level of $2-3 \times 10^{-18}\,B_\odot$ in each $1\ \mathrm{deg}^2$ area in the original data (outside the near-ecliptic bright zodiacal light) and the factor-of-3 increase expected from a tenfold change in the exposure time. In the brightest part of the zodiacal light, we anticipate the photon noise level being slightly higher according to the usual square root scaling—but no quiet period existed in this dataset in that portion of the image plane, so we confine ourselves to the out-of-ecliptic region shown in Figure 5.

We also note that the residual noise (visible in the accompanying movie) appears structured and the noisiest pixels are near the locations of stars in the original data stream. This implies that the dominant remaining noise term is errors in stellar photometry, which we attribute to the nonlinear response of the detector (it is thought to be nonlinear at the 0.5% level (C. Eyles 2009, private communication), though similar effects could arise from simple saturation of the individual detector pixels before on-board binning). This attribution is based on the observed fluctuation of the images at bright star locations, which varies faster than linearly with the star's intensity; and on the observation that the Milky Way imposes positive-definite artifacts on the resulting image stream.

3.3. The Limits of Heliospheric Imaging: Three-image Analysis of Contaminated Images

As a matter of interest, we now turn to an analysis of the bare minimum of image data required to perform background subtraction. This analysis demonstrates the limitations of a hypothetical *ground-based* heliospheric imager. Such an instrument would be subject to variable airglow effects similar to those imposed in Section 2.1 with levels of up to $10^{-13}\,B_\odot$, would also be limited both in cadence (to 24 hr) and in expected observing duration (to a stretch of at most a few consecutive days of ideal observing conditions). Despite these challenging limits, we demonstrate that it is possible to isolate celestial and airglow background sufficiently to locate a propagating CME, even with only a few images. Here we present the algorithmic steps required to treat images of this type, by isolating a propagating CME from just three of our

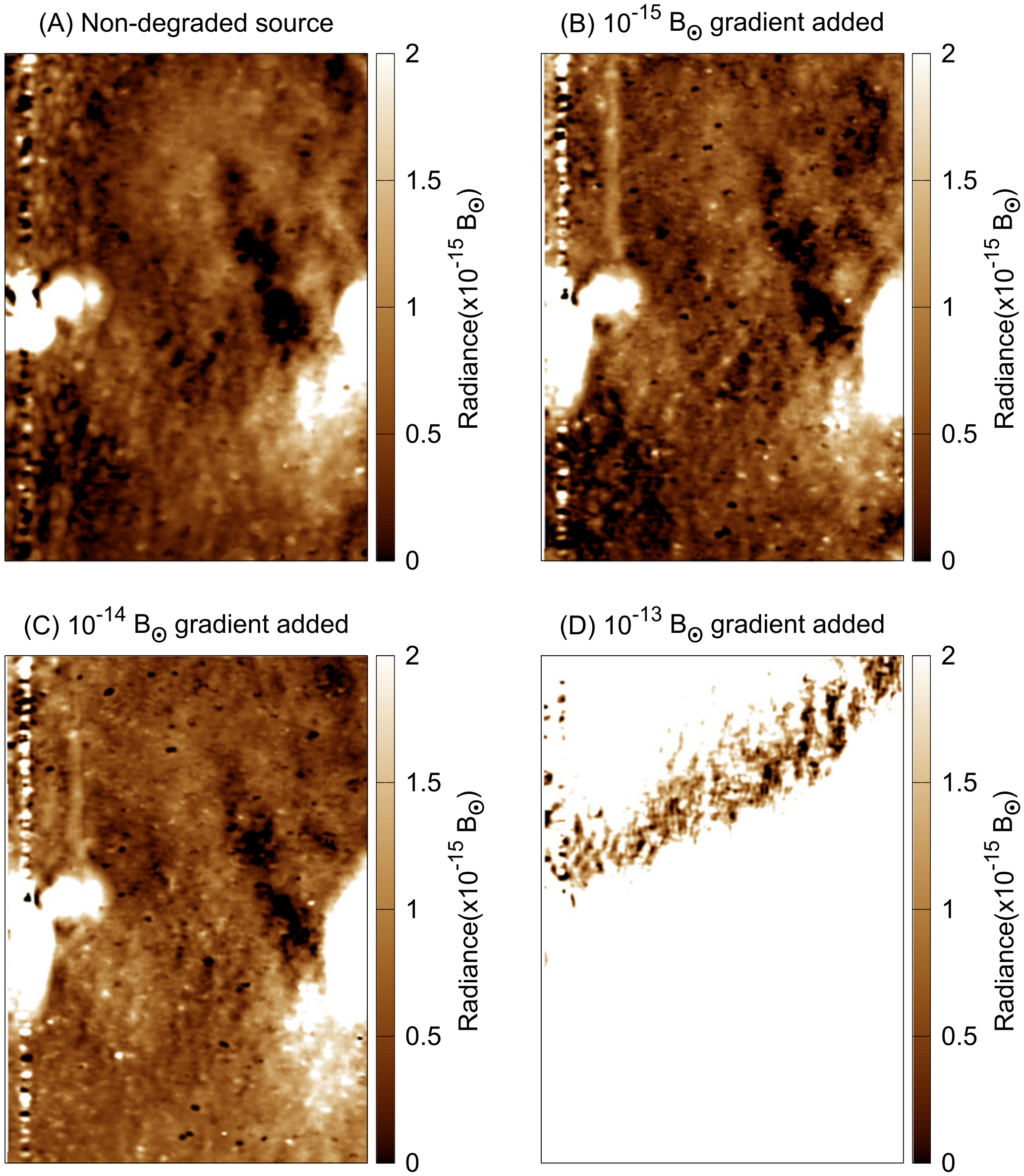

Figure 4. Extraction of features from variations of degradation of the HI-2 A image obtained on 2008 December 15 at 16:09UT (shown, with unmodified processing, in Figure 1 for comparison). Identical processing with the motion filter shown in Figure 3 was applied to all four data sets. (A) Undegraded data shows slightly worse results than the unmodified pipeline. (B) Addition of a randomized gradient at the 10^{-15} $B_{\odot}$ level does not significantly affect outcome. (C) Gradients at the 10^{-14} $B_{\odot}$ level moderately degrade the image. (D) Gradients at the 10^{-13} $B_{\odot}$ level overwhelm the simple filtration step. See also the Figure 4 movie in the digital version of this article.

experimental degraded heliospheric images from the 10^{-13} $B_{\odot}$ sequence that overwhelmed the simple filter described in Section 3.1. We used the three images collected by *STEREO/* HI-2 A at 2008 December 14 16:09, 2008 December 15 16:09, and 2008 December 16 16:09.

We first generated a zodiacal-light model using an analytic smoothing operation. We masked the images to eliminate the Earth occulter and the bright sunward edge of the FOV, took the pixelwise minimum value of the three masked images, median-filtered the resulting minimum-value image over a 21 pixel radius circle to reduce starfield effects, and then generated a quartic polynomial fit to the pixel value of each row of the image. This resulted in a 5 × 1024 array of quartic polynomial coefficients: one quartic per row of the smoothed-minimum image. We further smoothed these coefficients with a 75-row-wide median filter (i.e., each coefficient was replaced with the median value of the corresponding coefficient across 75 rows, truncated at the top and bottom edges of the array). Finally, we enumerated the quartic polynomial across columns to generate a 1024 × 1024 estimate of the zodiacal light. The zodiacal image is shown in Figure 6. As in the full treatment described in Section 3.1, we subtracted the zodiacal-light model from each of the three degraded images. The resulting image is shown in Figure 7.

As with the full treatment, we used patch correlation on an unsharp-masked copy of each zodiacal-subtracted image, to identify the coordinate transformation from each outlier image to the central one, then resampled to co-align the starfield. We subtracted the pixelwise average of the first and last images from the central one, to generate a running excess-brightness difference image. This image, shown in Figure 8, contains remnants of bright stars, both from detector

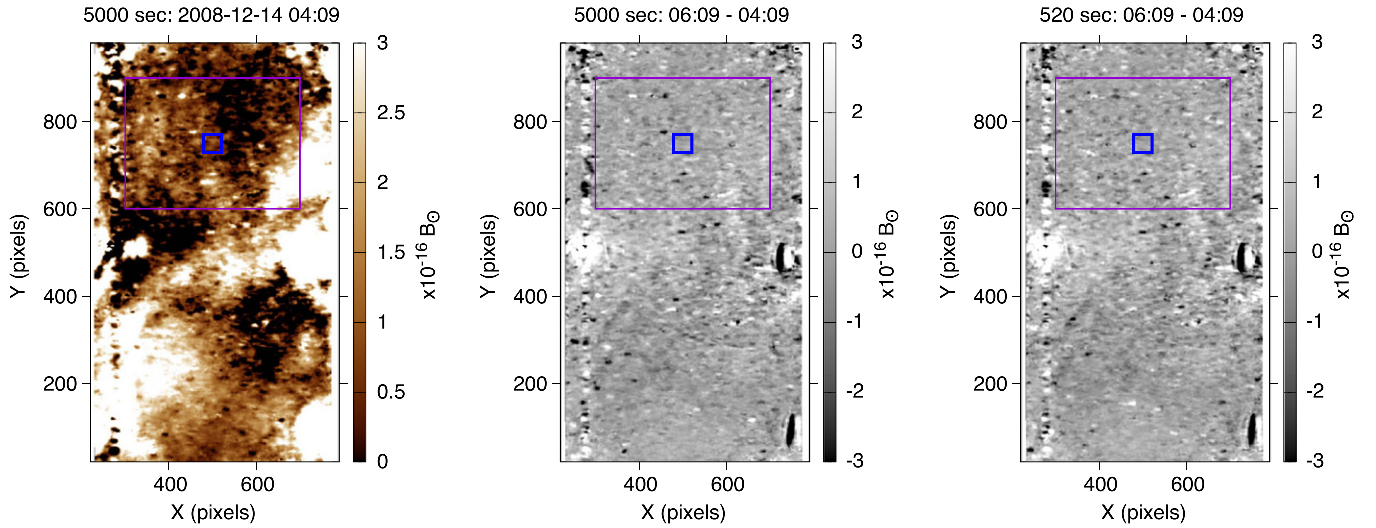

Figure 5. Noise level calculation uses differences between adjacent images in a quiet Sun region. Left: processed image of quiet Sun, with compressed dynamic range of $0{-}3 \times 10^{-16}\,B_\odot$. Center: difference image shows solar wind differences in the lower part of the image, and primarily noise in the upper part. Right: difference of two degraded images shows similar noise characteristics. The large purple box shows the quiet region for noise calculation; the small blue box marks a 1 degree square area.

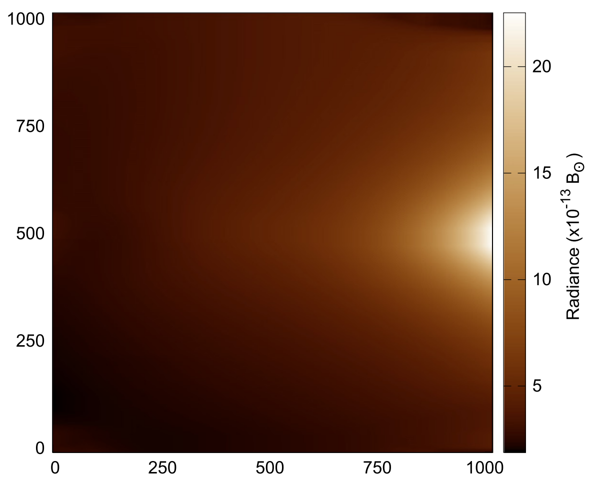

Figure 6. Zodiacal light estimate made from three degraded HI-2 images.

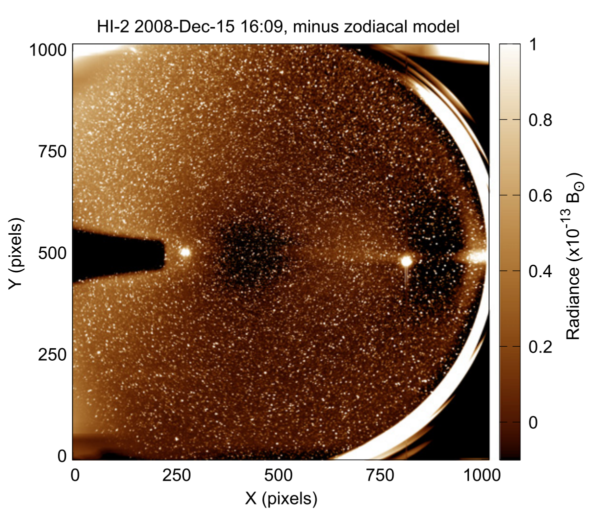

Figure 7. HI-2 image of 2008 December 15 16:09, after degradation, with the zodiacal light model of Figure 6 subtracted. Residual large-scale artifacts are visible due to the short baseline of the model, and to the multiple large-scale brightness patterns imposed on the three source images.

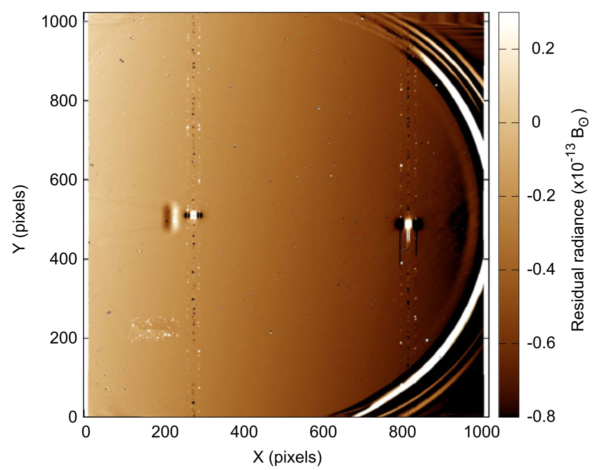

Figure 8. Starfield-subtracted triplet difference image reveals the imposed artifacts.

nonlinearities and from variations in the point-spread function (PSF) of the instrument. Further, it contains remnant gradients from the combined, imposed artifacts in each image.

The remaining background in Figure 8 has three principal components. First, regions where one or more images have bad values, including a data dropout around coordinates (200,200) and CCD bleed-through above Earth and Venus (at around x-value of 300 and 800 pixels, respectively), yield a "print-through" of the starfield. Second, the starfield subtraction yields blemishes due to nonlinearities in the detector sensitivity, and to variations in the PSF across the FOV. Third, our imposed artificial large-scale artifacts combine to produce a residual gradient across the FOV. The last two types of image feature have quite different spatial scales than the solar wind. The starfield blemishes have a spatial scale of a few pixels; our imposed gradient has a spatial scale of tens of degrees; and solar wind features have scales of 2°–20°. We separated these scales by first median-filtering with a 3° (42 pixel) diameter circular kernel to remove the residual starfield, then subtracting

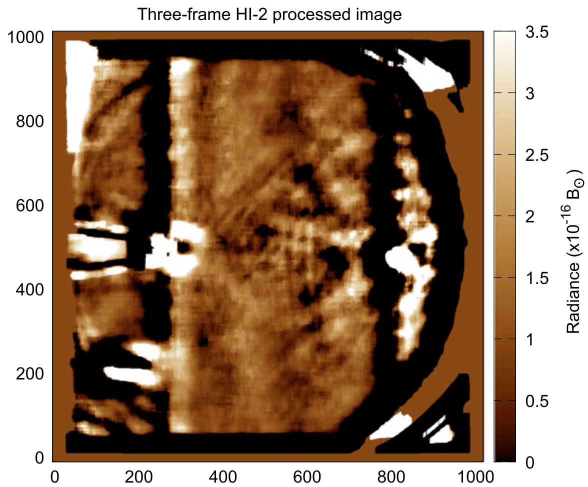

Figure 9. Processed triplet difference image reveals a CME roughly 45° from the Sun ($x = 600$–800), despite both imposed surface airglow contamination and the use of only three source images.

a large-scale background function made by convolving that smoothed image with a 12° half-width Gaussian kernel. The resulting processed difference image is in Figure 9. The CME is visible as a complex feature around $x = 400$–600 and we are able to track its location as it propagates, though here we could not recover photometric excess-radiance values as with full processing (e.g., DeForest et al. 2013).

We conclude that terrestrial heliospheric imaging at the image quality typical of pre-2011 analyses is likely possible, under ideal conditions, from a ground-based observatory. Terrestrial observing is not ideal for scientific or for space-weather monitoring purposes, given that far higher quality is now possible with the higher cadence and more reliable observing available even from LEO, but it is a useful proof-of-concept exercise. In particular, this analysis demonstrates the high relative importance of proper calibration and post-processing, compared to minimization of image contamination.

4. DISCUSSION AND CONCLUSIONS

We have analyzed the effect of three important types of degradation on heliospheric images, using post facto degradation of the high quality images from *STEREO*/HI-2: variable, diffuse background such as could be caused by stray light, airglow, or high altitude aurora; photon noise such as could be caused by shorter exposure time or lower instrument efficiency; and limited observation such as could be found from an extremely limited site, such a ground-based observatory.

We found that variable, diffuse backgrounds are easily removable, yielding quantitative images comparable to those created without such degradation, using a combination of gradient fits and removal of low-k, high-ω energy in the Fourier domain. Variable, diffuse backgrounds up to about $10^{-14}\,B_\odot$ (10% of the brightness of the zodiacal light) are easily removable to yield images with clear morphological indications of CME location and comparable photometry to that which can be obtained from undegraded *STEREO*/HI-2 images. Higher level gradients may be approachable with yet more careful analysis; this is hinted at by our three-image analysis, summarized below. Based on results of Sparrow et al. (1977) using the ten-color zodiacal light photometer on *Skylab*, the contamination due to geocorona at LEO altitudes is of the order of $10^{-15}\,B_\odot$; thus, this result indicates that geocorona effects in LEO would not adversely affect a potential LEO heliospheric imager.

We explored the effects of exposure time variations on heliospheric imaging. Based on a priori analysis, photon counting statistics appears not to be the major confounding factor in photometry from processed *STEREO*/HI-2 data; and we found, based on analysis of degraded images, that in fact photon statistics are not a major source of noise. We degraded a sequence of *STEREO*/HI-2 images to simulate exposure times nearly 10× shorter than the nominal 5000 s, and observed that the additional photon noise did not significantly change the frame-to-frame noise level in the processed data. From the small observed effect of photon noise increase, we conclude that photon noise is not a limiting factor in heliospheric imaging with current instruments.

As an exercise in limit-pushing, we explored the possibility of heliospheric imaging from an environment even more challenging than LEO: a ground-based exploratory measurement. We found that, even with the severe constraints imposed by a ground-based environment—i.e., cadence limited to 24 hr and potential observations limited to runs of 2–3 days—it should be possible, under ideal observing conditions, to image a CME at separations of 30° or more from the Sun, from a ground-based observatory. A demonstration observation, with post-processing as described in Section 3.3, could be expected to yield results comparable to those obtained routinely by SMEI during its mission. We do not advocate such an instrument to replace spaceborne monitoring, because limits imposed by the Moon, terrestrial weather, and low observing cadence would severely restrict the utility of such measurements as anything more than a demonstration.

Our analysis of degraded heliospheric images highlights the important balance between experiment design and post-processing as key elements of heliospheric feature detection and analysis. Heliospheric imaging is a very challenging photometric endeavor, as has been amply demonstrated elsewhere in the literature (e.g., Howard et al. 2013). We have already shown (DeForest et al. 2011) that *STEREO*/HI-2 is an appropriate and adequate instrument for wide-field white light imaging of the solar wind, given sufficiently careful post-processing of the image data stream. In this paper, we have demonstrated that *STEREO*/HI-2 is in fact *more* than adequate: a quantitative image signal can be extracted from a hypothetical wide-field imager with similar characteristics, located in a less favorable location (e.g., low Earth orbit) and/or with poorer photon statistics. In fact, the limiting element of the *STEREO*/HI-2 observations appears to be the photometric calibration: in particular, a combination of residual flat field errors and/or uncompensated detector nonlinearity form the current limits to full removal of the starfield a posteriori, by changing the instrument-reported brightness of each star as it crosses the pixel grid. These fluctuations, rather than photon noise, dominate the final noise level in processed HI-2 images.

Further, we have shown that even surprisingly bright variable diffuse background levels do not interfere significantly with photometric analysis of bright solar wind features such as CMEs, and even that non-quantitative imaging of CMEs (such as was achieved routinely from 800 km altitude by SMEI, e.g., Webb et al. 2006) should be possible, under ideal conditions, from a ground-based observatory.

The fact that we were able to remove even bright, randomly varying diffuse illumination at noise levels up to $10\times$ those of the brightest CMEs indicates that, with careful instrument characterization and similar post-processing to what we have developed, it would be possible to generate similar or superior photometric images of the solar wind even from low Earth orbit, despite vague warnings to the contrary in the literature (e.g., Jackson et al. 2010). This result further implies that, in optimizing a full heliospheric imaging effort, heroically deep baffling of stray light to the $10^{-17}\, B_{\odot}$ level is not necessary. It is only necessary to baffle stray light to levels comparable to (yet somewhat lower than) the existing zodiacal light in the FOV.

More broadly, our success in removing surprisingly large amounts of smooth background, and the result that photon noise is not the limiting factor for existing instruments, together highlight the importance of considering heliospheric imaging instruments and their post-processing algorithms as unified systems. Optimizing either part of the system to the detriment of the other will impact science adversely, and both should be considered jointly in designing new missions. Treating heliospheric imaging as a signal-processing problem with modern computers enables extraction of the heliospheric Thomson signal even under more challenging circumstances than those faced with *STEREO*.

REFERENCES

Brown, T. M., Kimble, R. A., Ferguson, H. C., Gardner, J. P., Collins, N. R., & Hill, R. S. 2000, AJ, 120, 1153

Byrne, J. P., Maloney, S. A., McAteer, R. T. J., Refojo, J. M., & Gallagher, P. T. 2010, NatCo, 1, 74

Davis, C. J., Davies, J. A., Lockwood, M., Rouillard, A. P., Eyles, C. J., & Harrison, R. A. 2009, GeoRL, 36, L08102

DeForest, C. E., Howard, T. A., & Matthaeus, W. H. 2013, in AGU 2013 Meeting of the Americas, Imaging the Variable Solar Wind (Cancun: AGU), SH31B-07

DeForest, C. E., Howard, T. A., & McComas, D. J. 2012, ApJ, 745, 36

DeForest, C. E., Howard, T. A., & McComas, D. J. 2013, ApJ, 769, 43

DeForest, C. E., Howard, T. A., & Tappin, S. J. 2011, ApJ, 738, 103

Eyles, C. J., Harrison, R. A., Davis, C. J., et al. 2009, SoPh, 254, 387

Eyles, C. J., Simnett, G. M., Cooke, M. P., et al. 2003, SoPh, 217, 319

Harrison, R. A., Davis, C. J., Eyles, C. J., et al. 2008, SoPh, 247, 171

Howard, T. A., Bisi, M. M., Buffington, A., et al. 2013, SSRv, 180, 1

Howard, T. A., & DeForest, C. E. 2012, ApJ, 752, 130

Howard, T. A., & DeForest, C. E. 2012, ApJ, 746, 64

Howard, T. A., & Tappin, S. J. 2009, SSRv, 147, 31

Jackson, B. V., Buffington, A., Hick, P. P., Bisi, M. M., & Clover, J. M. 2010, SoPh, 265, 257

Jackson, B. V., Buffington, A., Hick, P. P., Wang, X., & Webb, D. F. 2006, JGR, 111, A04S91

Jackson, B. V., & Leinert, C. 1985, JGR, 90, 10759

Jursa, A. S. (ed.) 1985, in Handbook of Geophysics and the Space Environment

Liu, Y., Davies, J. A., Luhmann, J. G., et al. 2010, ApJL, 759, 68

Lugaz, N. 2010, SoPh, 267, 411

Lugaz, N., Vourlidas, A., Roussev, I. I., et al. 2008, ApJL, 684, L111

Mizuno, D. R., Buffington, A., Cooke, M. P., et al. 2005, JGR, 110, A07230

Möstl, C., Temmer, M., Rollett, T., et al. 2010, GeoRL, 37, L24103

Roach, F. E. (ed.) 1973, in The Light of the Night Sky (Dordrecht: Reidel), 28

Rouillard, A. P., Davies, J. A., Forsyth, R. J., et al. 2008, GeoRL, 35, L10110

Sheeley, N. R., Jr., Herbst, A. D., Palatchi, C. A., et al. 2008, ApJ, 675, 853

Sheeley, N. R., Jr., & Rouillard, A. P. 2010, ApJ, 715, 300

Sheeley, N. R., Jr., Wang, Y.-M., Hawley, S. H., et al. 1997, ApJ, 484, 472

Sparrow, J. G., Weinberg, J. L., & Hahn, R. C. 1977, ApOpt, 16, 978

Tappin, S. J., & Howard, T. A. 2009, ApJ, 702, 862

Vourlidas, A., & Howard, R. A. 2006, ApJ, 642, 1216

Webb, D. F., Mizuno, D. R., Buffington, A., et al. 2006, JGR, 111, A12101

Weinberg, J. L., Hahn, R. C., & Sparrow, J. G. 1975, SSI, 1, 407

Wood, B. E., Wu, C.-C., Howard, R. A., Socker, D. G., & Rouillard, A. P. 2011, ApJ, 729, 70